# Chapter 20
# Transmission Electron Microscopy

## 20-1 INTRODUCTION

Transmission electron microscopy (TEM) is the pre-eminent method for determining dislocations' and other crystallographic defects' character and for performing chemical and crystallographic analysis of micrometer and smaller precipitates and other microstructures. Use of TEM in materials science/engineering can be introduced here n only a few additional pages and is well worth the small increment of effort. Since most defect characterization requires an understanding of diffraction contrast, this is an important constituent of this chapter.

Already Sec. 3-9 showed how a TEM can be used to image either a planar section through reciprocal space (i.e., the diffraction pattern) or the sample itself. Section 17-3 discussed how diffraction contrast could be used to identify defect character; this introduction was in the context of x-ray diffraction topography, the x-ray imaging analog of TEM. The treatment of TEM, therefore, builds on what was already presented, with the four sections on the TEM, its components and operation followed by four sections on analysis of information obtained using TEM.

Section 20-2 discusses the interaction of electrons with electric and magnetic fields, Sec. 20-3 covers electron guns (i.e., sources), Sec. 20-4 discusses magnetic lenses and Sec. 20-5 introduces electron optics, focusing on the lenses in a generic TEM and their differences from glass lenses used in optical microscopes. The subject of Sec. 20-6 is Kikuchi lines, of Sec. 20-7 is convergent beam diffraction, of Sec. 20-8 is imaging and amplitude contrast and of Sec. 20-9 is imaging and phase contrast.

## 20-2 ELECTRON INTERACTIONS WITH ELECTRIC AND MAGNETIC FIELDS

In an electric field $\mathbf{E}$ and magnetic field $\mathbf{H}$, the electrons experience the Lorentz force $\mathbf{F}$ given by

$$\mathbf{F} = -e(\mathbf{E} + \mathbf{v} \times \mathbf{H}) \tag{20-1}$$

where $e$ is the charge and $\mathbf{v}$ is the velocity vector of the electron. When combined with Newton's expression

$$\mathbf{F} = m\mathbf{a} = md^2\mathbf{x}/dt^2, \tag{20-2}$$

where $t$ denotes time and $m$ is the mass, $\mathbf{a}$ is the acceleration vector and $\mathbf{x}$ is the position vector of the electron, an expression for particle optics results. In TEM, the first term of Eq. 20-1, the electric field interaction, applies to the electron gun where the electrons produced by the filament are accelerated to the energy to be used in the microscope. The second term of Eq. 20-1, describing the magnetic field interaction, governs the operation of TEM lenses. In particular, it is important to remember that the spatial variation of $\mathbf{E}$ and $\mathbf{H}$ is essential in the operation of the TEM electron gun and lenses.

## ELECTRON GUN

Figure 20-1 shows a schematic of an electron gun. The filament is the cathode (C in Fig. 20-1) and is at a potential $\phi_C = -U$ relative to the anode A (i.e., $\phi_A = 0$). Many of the electrons emitted from the filament strike the anode and are lost, but some pass through the hole and proceed along the optic axis. Between the cathode and anode, the cup-like Wehnelt cylinder improves the uniformity of electron emission from the gun: the cylinder has a slight positive bias $\phi_W$ with respect to the cathode.

The relationship between $\mathbf{E}$ and the potential is

$$\mathbf{E} = -\nabla\phi = -(\partial\phi/\partial x, \partial\phi/\partial y, \partial\phi/\partial z) \tag{20-3}$$

lines of constant potential $\phi$ appear in Fig. 20-1(a), and the corresponding electron trajectories are shown in Fig. 20-1(b). Control of the electron trajectories within the gun are important in obtaining good imaging performance, but the energy of the electrons depends only on the potential through which they are accelerated not

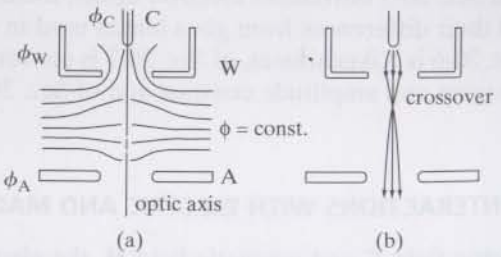


**Figure 20-1** Illustration of the electron gun. (a) Lines of constant potential $\phi$ and (b) electron trajectories in relation to the cathode C, the Wehnelt cylinder W, and anode A. After [20.7].



their trajectories. Acceleration through 100 kV produces electrons with 100 keV energy, and the relationship between accelerating potential and electron wavelength $\lambda$, correcting for relativistic effects, is

$$\lambda = h[2m_0 eU(1 + eU/\{2 m_0 c^2\})]^{-0.5}, \tag{20-4}$$

where $m_0$ is the electron rest mass, $c$ is the speed of light and $h$ is Planck's constant. Accelerating potentials of 100 kV or greater are normally used, and Table 20.1 lists potentials and corresponding wavelengths. Note that, unlike in x-ray diffraction, wavelengths and $d$-spacings in electron microscopy conventionally are given in nm.

Filaments can be made from W or more exotic materials such as $LaB_6$. In most TEM's, electrons are produced by thermionic emission as they are in x-ray tubes. Field emission of electrons from a very sharp W tip can also be used in the gun; no heating is required. Field emission guns provide much greater current density but require a much better vacuum than thermionic emission guns.

## 20-4 MAGNETIC LENSES

In considering the operation of the magnetic lenses of a TEM, the focus is on the second term of Eq. 20-1 which states that the force $\mathbf{F}$ from a magnetic field $\mathbf{H}$ on an electron moving with velocity $\mathbf{v}$ is perpendicular to both $\mathbf{v}$ and the component of $\mathbf{H}$ perpendicular to $\mathbf{v}$. Note that any component of $\mathbf{H}$ parallel to $\mathbf{v}$ produces no force. If $\mathbf{v} \perp \mathbf{H}$, a circular trajectory results. More complex helical paths result when uniform motion along the field is superimposed on uniform rotation in the plane perpendicular to the field. This occurs when $\mathbf{v}$ makes a slight angle $\alpha$ with the magnetic field $\mathbf{H}$ (Fig. 20-2(a)); at $z$=0 the electron is $r$ away from the $\mathbf{z}$-axis, and the force at any instant deflects the electron toward the $\mathbf{z}$-axis (in a direction out of the plane of the page) as it spirals around a cylinder of radius $r$.

A spatially varying magnetic field is required for focusing, and a typical field distribution is shown in Fig. 20-2(b) for a magnetic lens. The $\mathbf{z}$-axis is the center of the cylindrically symmetric lens, and $\mathbf{H}$ has mirror symmetry across the plane $z$=0. Below the diagram of $\mathbf{H}(r,z)$, the values of the components $H_z$ and $H_r$ are plotted

**Table 20.1**

| Accelerating voltage (kV) | Wavelength (nm) |
|---|---|
| 100 | 0.00370 |
| 150 | 0.00335 |
| 200 | 0.00251 |
| 300 | 0.00197 |
| 400 | 0.00164 |
| 1000 | 0.00087 |

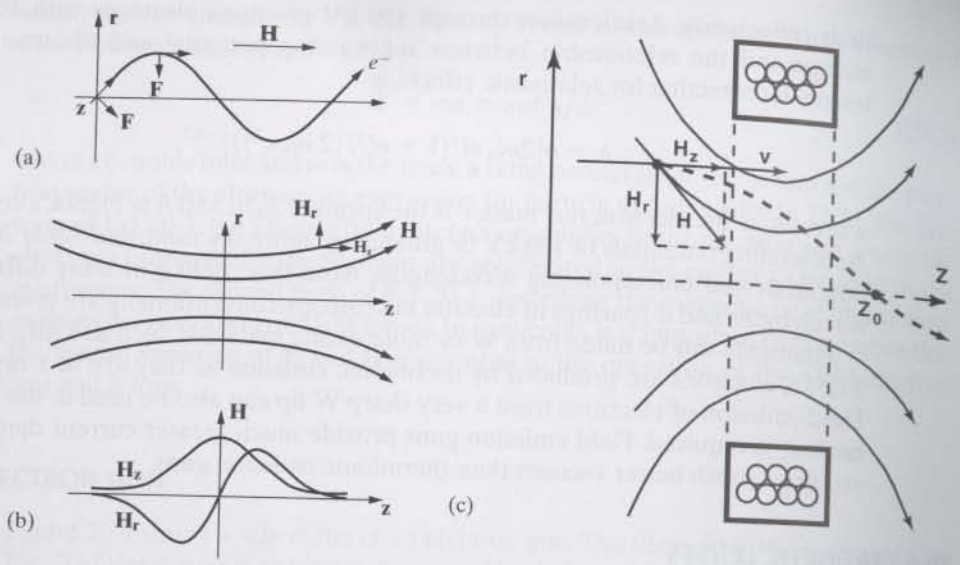


**Figure 20-2** (a) Projection of the electron trajectory in a constant magnetic field **H**, with the direction of the force **F** on the electron indicated. (b) Variation of **H** in a magnetic lens, showing components $\mathbf{H}_r$ and $\mathbf{H}_z$ (radial and along the optic axis, respectively), as a function of z. (c) Projection of the electron path on the initial plane, showing lenses and crossover point $\mathbf{z}_0$. After [20.1].

for a position near the optic axis (i.e., $r$ approaching 0). This magnetic field distribution is obtained using a coil carrying electrical current centered on the optic axis (Fig. 20-3). The gap in the iron pole piece containing the windings allows magnetic field leakage not only directly across the gap but also out into the bore of the pole piece. The design of magnetic lenses has become quite sophisticated, and more detailed discussion of lenses and their design appears in texts on electron microscopy [20.1, 20.2].

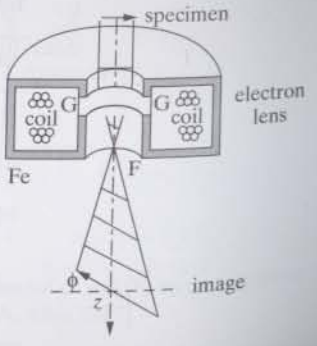


**Figure 20-3** Illustration of concentration of a rotationally symmetric magnetic field by the gap in the electron lens and the resulting image rotation. After [20.7].



The dashed line in Fig. 20-2(c) illustrates schematically the trajectory of electrons traveling parallel to but off of the optic axis. Actually, the electron spirals toward the optic axis and then crosses it with $r$ steadily decreasing and then increasing again; therefore, the dashed line is the projection of the electron's path onto the initial plane $(r,z)$ containing the electron. The closer the electrons are to the optic axis, the smaller their deflection, and electrons traveling exactly on the optic axis experience no deflection. Note that the electrons off the plane shown and off the optic axis in Fig. 20-2(c) also spiral toward the optic axis. If the focussing action of the lens is perfect, all of the electrons traveling parallel to **z** and lying on the plane intersecting the page along the line $z = z'$ (Fig. 20-2(c) will converge to a point at $z = z_0$, and the line $z = z'$ will rotate as the electrons travel through the lens (Fig. 20-3). In other words, the image of the sample formed by the electrons rotates as it travels through the lens. If the strength of the lens changes, i.e., if **H** increases or decreases, the amount rotation will alter must be known for correct interpretation of diffraction patterns and images. This rotation is not present in glasses lenses.

Various aberrations exist in all lenses, to a greater or lesser degree, and spherical and chromatic aberrations, astigmatism and distortion all contribute to degrading image quality. Spherical aberration results because the lens field acts inhomogeneously on electrons following off-axis paths and spreads the image of a point into a disk. Chromatic aberration exists because a lens deflects lower energy electrons more strongly than higher energy electrons; the range of energy $\Delta E < 1$ eV for the incident beam and increases to 15-20 eV for some of the electrons emerging from a 50-100 nm thick sample [20.2]. Astigmatism arises from the inevitable deviations of the lens from cylindrical symmetry. Finally, image distortion can sometimes occur, e.g., a set of orthogonal lines can appear concave inward to the center of the image (pincushion) or bulge outward (barrel).

## 20-5 TRANSMISSION ELECTRON MICROSCOPES

Any TEM is a complex assembly of magnetic lenses (in addition to an electron gun described in Sec. 20-3), several apertures, a sample holder and an image recording/viewing system (Fig. 20-4). The magnetic lenses can be grouped into those of the illumination system between the electron gun and sample and those of the imaging system after the sample. Typically one finds two condenser lenses in the illumination system and three lenses in the imaging system; the descriptions below refer to this kind of TEM.

Consider first the illumination system. The traditional TEM mode adjusts two condenser lenses to illuminate the sample with a nearly parallel beam (convergence angle $\alpha < 10^{-4}$ rad compared to electron diffraction angles on the order of $10^{-2}$ rad). This beam covers sample areas several micrometers in diameter at magnifications between 20,000X and 100,000X. Without the action of the condenser lens concentrating the electron beam into the area of interest, the images would be too dim to be useful. For applications other than imaging, highly convergent beams can be produced, but discussion of this is postponed until Sec. 20-7. Pre-specimen scanning

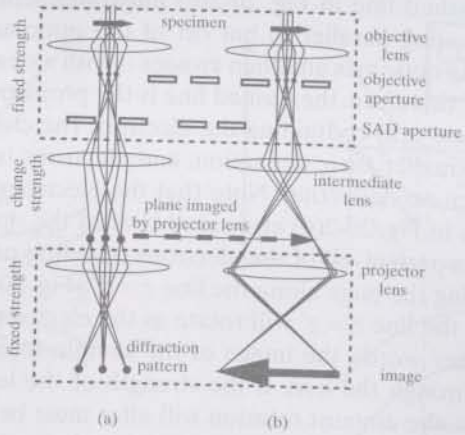


**Figure 20-4** Ray diagram for viewing the diffraction pattern (a) and the image of the sample (b). The strength of the intermediate lens is changed to focus on the back focal plane or on the image plane, respectively. After [20.2].

or deflection coils are often used to control beam position or angle.

When the electrons encounter the sample, some are diffracted in various directions depending on the orientation of the crystal(s) through which the incident beam travels. Section 3-9 details the formation of the diffraction pattern, i.e., the action of the objective lens bringing parallel rays to a point focus in the back focal plane (see also Fig. 20-4). Section 3-9 also describes how the objective lens simultaneously brings differently directed rays (that is, electrons) emanating from a single point on the sample back to a single point in the first intermediate image plane.

In TEM one can switch between imaging the sample and viewing its diffraction pattern by changing the strength of the intermediate lens. To see the diffraction pattern, the intermediate lens is adjusted to focus on the back focal plane of the objective lens; i.e., the back focal plane acts as the object plane for the intermediate lens. In the imaging mode the intermediate lens is adjusted so that its object plane is the image plane of the objective lens.

When viewing a diffraction pattern, an aperture limiting the area contributing to the pattern is typically inserted into the first intermediate image plane; this diffraction mode is therefore called selected area diffraction or SAD, and the aperture is called the SAD aperture. While SAD is the most common diffraction mode, other modes including convergent beam diffraction can be very valuable. A typical SAD pattern was shown in Fig. 3-24, and experienced microscopists can readily recognize patterns recorded with the electron beam along high symmetry, low index directions.

Depending on the amount of magnification provided by the intermediate and projector lenses, 1 cm on the diffraction pattern recorded on film may correspond to various $nm^{-1}$. Convenience dictates using standardized settings for most work,



and the camera length $L$ is used to describe the magnification of the diffraction pattern. While $L$ is a calculated rather than a physical distance, the concept of a camera length arose from x-ray diffraction projection cameras which operate without lenses and in which the diffraction pattern is magnified by moving the recording medium farther from the sample. Figure 20-5 shows the Ewald sphere construction and the direct space diagram relating distance $R$ between the incident beam **O** and the diffracted beam **G** (on the film) and the camera length $L$. From the figure,

$$\tan 2\theta_{hkl} = R/L = (1/d)/(1/\lambda)$$

and

$$Rd = \lambda L \tag{20-5}$$

with $\lambda$ and $L$ known from the TEM's operating parameters, simple measurement of distances $R$ on the film is sufficient to determine $d$ for the diffraction spot of interest. Each investigator should do this calibration for her- or himself and should not rely on factory calibrations because the conditions used may be different. If the sample is of a known material, the indices of two non-collinear spots $\mathbf{G}_1$ and $\mathbf{G}_2$ can be quickly assigned, and the incident beam direction **B** can be determined from the cross product of $\mathbf{G}_1$ and $\mathbf{G}_2$. An example is provided in Fig. 20-6.

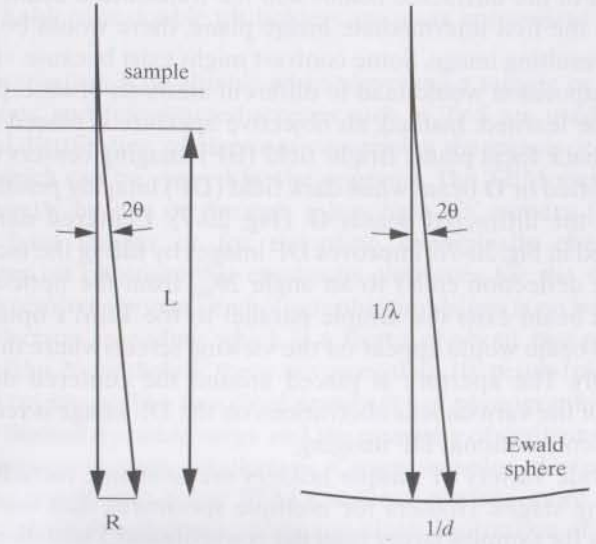


**Figure 20-5** Direct space and reciprocal space illustrations of the camera length L.

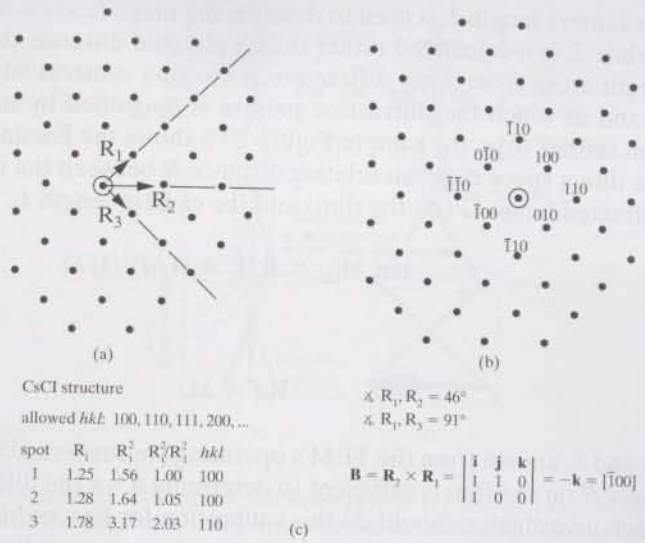


**Figure 20-6** Indexing the diffraction pattern shown in Fig. 3-24 (NiAl which has the CsCl structure). The diffraction pattern is reproduced in (a), and a schematic of it appears in (b) with separations $R_i$ between O and three diffracted beams indicated. In (c) the values of $R_i^2$ and of the angles between $R_i$ are used to determine the incident beam direction **B**. The resulting indices for several diffraction spots are shown in (b).

If all of the diffracted beams and the transmitted beam were allowed to recombine in the first intermediate image plane, there would be relatively little contrast in the resulting image. Some contrast might exist because varying thickness or varying composition would lead to different amounts of absorption, but relatively little could be learned. Instead, an objective aperture is placed around one of the spots in the back focal plane. Bright field (BF) imaging centers the aperture around the transmitted or **O** beam while dark field (DF) imaging positions the aperture around one of the diffracted beams $\mathbf{G}_i$ (Fig. 20-7). Centered dark field (CDF) imaging, depicted in Fig. 20-7b, improves DF images by tilting the incident beam (via the presample deflection coils) to an angle $2\theta_{hkl}$ from the optic axis so that the *hkl* diffracted beam exits the sample parallel to the TEM's optic axis. Thus, the *hkl* diffracted beam would appear on the viewing screen where the **O** beam would be seen normally. The aperture is placed around the centered diffracted beam, and the effect of the various lens aberrations on the DF image is reduced considerably from that in conventional DF imaging.

A wide variety of sample holders are available including heating, cooling and straining stages. Holders for multiple specimens find use as well as bulk sample holders for samples larger than the conventional 3 mm diameter disks. Most TEM's now incorporate side entry specimen holders, and these provide at least one axis of sample rotation (about the axis of the rod-like holder). This single degree of freedom is enough to allow identification of defect character in some cases. Often, however, tilt-rotate holders or double tilt holders are more convenient for defect studies.



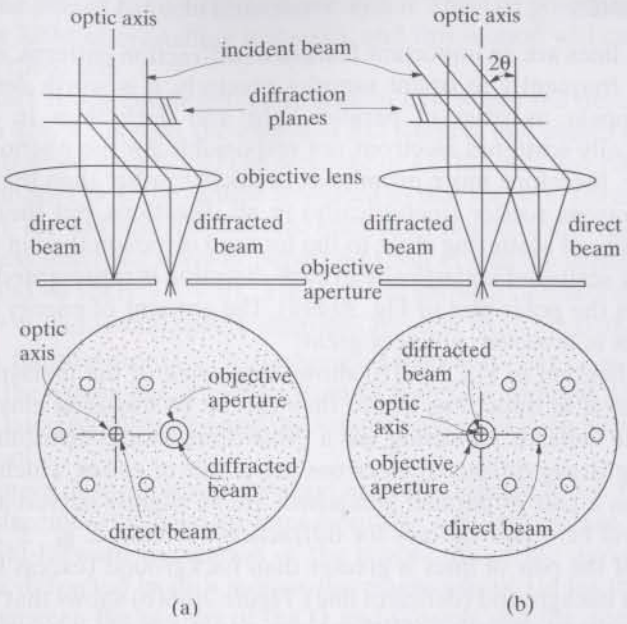


**Figure 20-7** Aperture position and ray paths for (a) conventional dark field (DF) imaging and (b) centered dark field (CDF) imaging.

Real time observation is invaluable when surveying a sample or when adjusting viewing conditions, and fine-grained screens such as ZnS are used to convert the two-dimensional distribution of electrons comprising the image or diffraction pattern into light which can be viewed by the operator. The TEM viewing screen can be observed directly by eye or through a low light TV camera (which is a real advantage for faint images or for recording dynamically changing images). Recording images on photographic emulsions continues for the vast majority of TEM work. The resolving power of photographic emulsions is no better than about 10 $\mu$m due to electron spreading which is a factor of about two greater than the grain size of the film. Nonetheless, there are more than $10^7$ pixels (picture elements) in a 10 cm $\times$ 10 cm image. The two chief drawbacks of photographic emulsions are their inherently limited dynamic range and the necessity of digitizing the images for quantitative comparison with simulations. Charge-coupled device (CCD) chips have been incorporated into a few TEM's and can provide more than $10^6$ pixels, orders of magnitude higher dynamic range and direct digitization of images (Secs. 1-8 and 6-10). Conventional read-out speeds of CCDs and related detector arrays can be bothersomely slow for viewing, but most chips allow rapid, albeit noisy readout.

## 20-6 KIKUCHI LINES

Kikuchi lines are an important feature of diffraction patterns, and, because they are used so frequently to orient samples precisely, it is worth describing their origin. They appear as pairs of parallel light and dark lines in diffraction patterns. Inelastically scattered electrons are responsible for the phenomenon, and Kikuchi lines are, therefore, more prominent in thicker rather than thinner sections of foils. The electrons scatter (inelastically) in all directions, but there is a much greater probability of scattering close to the forward direction than in other directions. The intensity scattered inelastically in each direction is represented by the length of the vector in the polar plot of Fig. 20-8(a). The amount of energy lost by the scattered electrons is, however, not very great.

The diagram in Fig. 20-8(b) shows that some of the inelastically scattered electrons travel in directions where they can be re-scattered elastically through $2\theta_{hkl}$. Since the inelastic scattering has a three-dimensional distribution, the locus of the resulting Bragg diffracted electrons are a pair of cones, which intersect the Ewald sphere as a pair of parallel arcs which are so slightly curved as to appear straight. There will be a pair of lines for diffraction vectors $\pm$ **g**, $\pm$ **2g**, etc. The intensity of one of the pair of lines is greater than background (excess line) and the other is less than background (deficient line). Figure 20-8(b) shows that the inelastically scattered electrons on path 1 (OB) are closer to the incident beam direction than those along path 2 (OA); before the second scattering event (diffraction), the intensity along path 1 is higher. Diffraction redirects the intensities as shown in Fig. 20-8(b), and the result is that the left-most Kikuchi line, from path 1, has the larger intensity.

Geometry dictates that the projection of (*hkl*) lies midway between the excess and deficient (*hkl* and $\overline{hkl}$, respectively) Kikuchi lines. The angle between the excess and deficient lines is twice the Bragg angle and not four times the Bragg angle. As the crystal is rotated, the projection of (*hkl*) onto the diffraction pattern

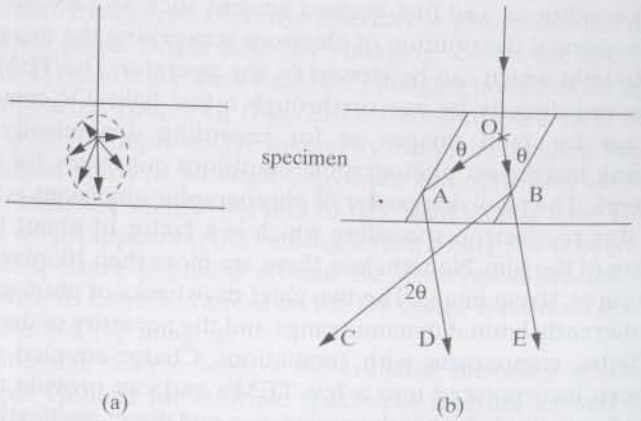


(a) (b)

**Figure 20-8** Simplified illustration of the production of Kikuchi lines. (a) Polar plot of the magnitude of inelastic electron scattering as a function of scattering angle. (b) Diffraction of the inelastically scattered electrons and the production of excess and deficient lines.



moves and the pair of Kikuchi lines move with it. This last point has enormous consequences in TEM of crystalline materials, and this section will end with a discussion of what these are.

At the exact Bragg condition for reflection *hkl*, where the deviation parameter $s$ defined in Sec. 5-3 is zero, the excess or *hkl* Kikuchi line passes through the center of the diffraction spot **G** and the deficient or $\overline{hkl}$ Kikuchi line passes through the incident beam spot **O**. If the sample is rotated so that the direct beam is exactly parallel to (*hkl*), the *hkl* and $\overline{hkl}$ Kikuchi lines are symmetrically displaced about **O** with the excess line lying midway between **O** and G and the deficient line midway between **O** and -**G** (here $s < 0$).[1] Figure 20-9a shows a diffraction pattern recorded with $s > 0$, and Ewald sphere diagrams for $s < 0$, , $s = 0$ and $s > 0$ appear in Fig. 20-9b. In other words, $s > 0$ whenever the excess line is on the same side of **O** as **G** and the excess line is farther from **O** than **G**. Optimum defect contrast, as will be seen later, requires aligning the sample to certain $s$ so Kikuchi lines are an invaluable tool.

Small changes in specimen orientation are very difficult to see in SAD patterns, but the displacement of Kikuchi lines from the spot centers are easy to see and allows straight-forward calculation of the magnitude of the deviation parameter. Knowing the diffracted beam's indices, the magnitude of $1/d$ for the reflection, the separation between the centers of the **O** and **G** spots and the displacement of the pair of Kikuchi lines from their positions at $s = 0$ and forming appropriate ratios allows calculation of the magnitude of $s$.

So far the discussion focused on one pair of Kikuchi lines, but many pairs appear simultaneously especially when the beam direction **B** is close to a low index direction. The pattern of Kikuchi lines reflects the symmetry of the crystal, and Kikuchi maps are often constructed to help microscopists rotate/tilt from one low index **B** to another. With the TEM in the SAD mode, a pair of Kikuchi lines leading to the desired low index direction are found and followed to the desired low index direction. One essentially "drives" along the lines by rotating/tilting the crystal. Some workers find it faster to construct a stereographic projection representing the foil orientation (if **B** is at the center of the projection, the various **G** in the diffraction pattern lie on the projection's perimeter) and to use it to tilt directly to the new

## 20-7 CONVERGENT BEAM DIFFRACTION PATTERNS

Convergent beam electron diffraction (CBED) offers considerable advantages over SAD, and its development transformed electron crystallography into a technique with power comparable to neutron or x-ray crystallography. To demonstrate how features arise within CBED patterns, differences between CBED and SAD are discussed first, the existence of higher order diffraction zones are described

[1] In this geometry the simple model of excess and deficient lines presented above predicts that the lines will have intensities indistinguishable from the background. The lines are visible, however, and a more complex explanation is required than can be presented here.

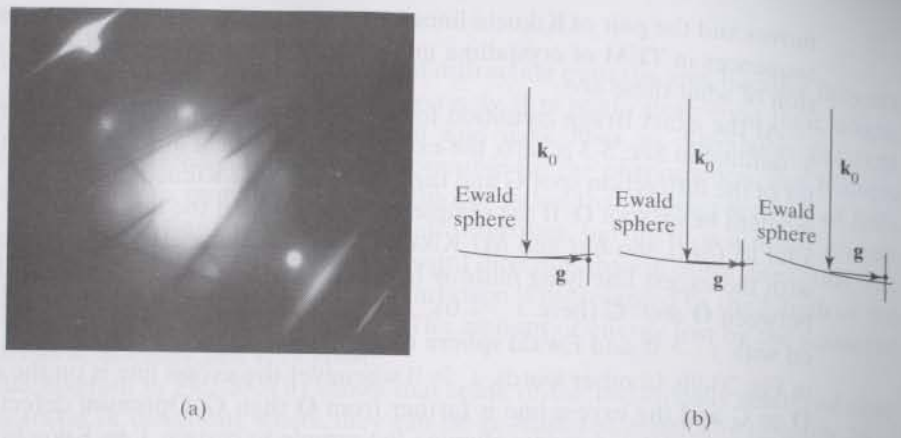


(a) (b)

**Figure 20-9** (a) Diffraction pattern recorded with the deviation parameter of greater than zero. (b) Orientation of the incident beam, the Ewald sphere, **g** and *hkl* relrod for deviation parameter less than zero (left), equal to zero (middle) and greater than zero (right).

next and the use of higher order Kikuchi lines to determine point and space groups is covered last.

A spatially wide (1 − 10 $\mu$m diameter) nearly parallel beam (with a single incident wave vector **k** and a very small convergence angle $\alpha$) is normally used in SAD while CBED uses a convergent beam (range of **k** and $2\alpha \lesssim 2\theta_B$) and a relatively small area ( ~ 10 − 100 nm diameter). Parallel illumination means that an SAD pattern consists of an array of sharp maxima in the back focal plane of the objective lens. A convergent beam, however, produces disks of high intensity in the back focal plane, and at some point, increasing $\alpha$ leads to overlap of disks. For thin samples, kinematical diffraction dominates and the disks are featureless. Thicker samples allow dynamical diffraction effects to be observed, and complex contrast appears within the disks. Figure 20-10 compares a 111 SAD pattern from Si and the corresponding CBED pattern, and both are most useful when **B** is along a zone axis of the crystal.

To understand the origin of the dark lines in the CBED disks, one needs to consider diffraction spots other than those near the direct beam. The section of the Ewald sphere in Fig. 20-11(a) shows the incident beam along 001 and demonstrates that the diffraction spots near the incident beam are from relrods extending from the *hk*0 plane. The farther from **O**, the farther the Ewald sphere curves from (*hk*0), until the *hk*0 spots from the zero order Laue zone (ZOLZ) are no longer prominent. Still farther from the origin of reciprocal space, the relrods from the *hk*1 reciprocal lattice plane begin to intersect the Ewald sphere and produce the spots of the first order Laue Zone (FOLZ). Normally, SAD and CBED patterns do not include FOLZ spots because the camera length $L$ is too large, i.e., the angular field of view is too small to record these large reciprocal distances (Fig. 20-11(b).



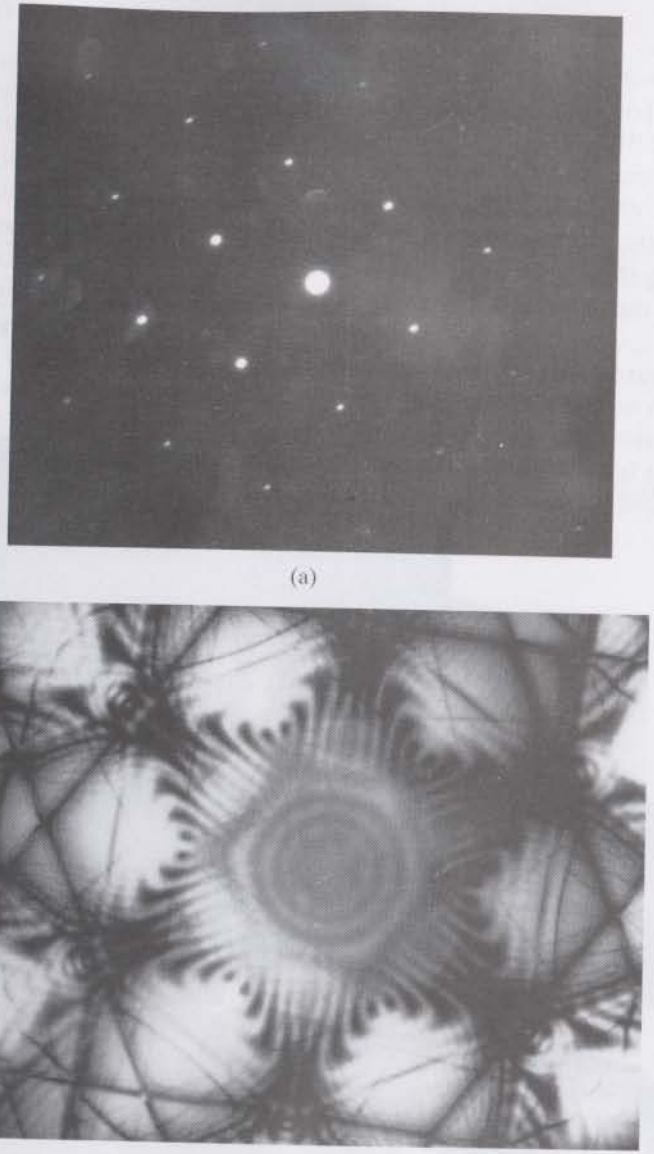

(a) (b)

**Figure 20-10** Silicon 111 diffraction patterns: (a) Selected area diffraction (SAD) pattern and (b) Convergent beam electron diffraction (CBED) pattern.

Each of the FOLZ and higher order Laue zones (HOLZ) reflections has Kikuchi lines associated with them. In zone axis patterns, many reflections appear at the exact Bragg condition, including HOLZ reflections which have small $s$. The excess HOLZ Kikuchi lines, as well as the HOLZ spots, are outside the image field

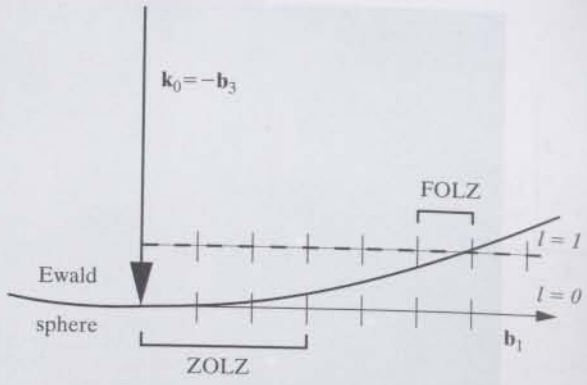


(a)

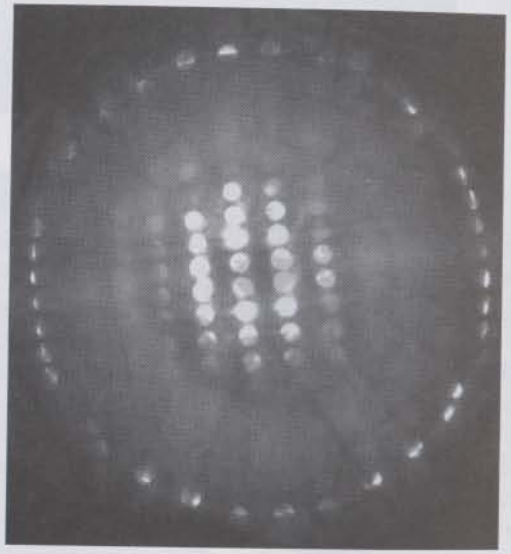

(b)

**Figure 20-11** Origin of the zero order Laue zone (ZOLZ) and first order Laue zone (FOLZ). (a) Section of reciprocal lattice showing intersection of relrods in ZOLZ and FOLZ. (b) Diffraction pattern recorded with a much smaller than normal camera length L and showing appearance of the Laue zones.

normally used in CBED while the deficient Kikuchi lines lie near the direct beam; in fact the deficient HOLZ Kikuchi lines cut the disks of the CBED pattern. The symmetry of the HOLZ lines reflects the space group of the sample: the three-dimensional crystallography of the sample can be inferred because the HOLZ lines include information off the *hk*0 plane of the reciprocal lattice. Exactly how this is done and how foil thickness is precisely measured is thoroughly covered elsewhere [20.2, 20.3].



## 20-8 IMAGING AND AMPLITUDE CONTRAST

As mentioned in Sec. 20-5, defect characterization is normally done by allowing only one beam to form the image: the objective aperture is centered around either the transmitted beam **O** for BF imaging or a diffracted beam for DF imaging. Good defect visibility results for two-beam conditions, that is, when the crystal is tilted so that only one diffracted beam has $s \sim 0$ and has strong intensity and the other diffracted beams have $s \ll 0$ or $s \gg 0$. The length of the relrods, due to the small sample thickness normal to the plane of the foil, dictates that SAD patterns never consist of only two spots, but the intensity of one diffracted beam can be made much stronger than that of all of the others.

During a typical TEM session, the microscopist finds a transparent area of the sample and alters the specimen orientation until a low-index zone axis is seen in SAD pattern. This assumes, of course, that there are features of interest to be seen. Slight tilts from the zone axis are then required to obtain several different two-beam conditions. For an incident beam direction $\mathbf{B} = [001]$, $\mathbf{g} = [200]$, $[020]$, $[110]$, and $[\bar{1}10]$ are readily obtained two-beam conditions (Fig. 20-12).

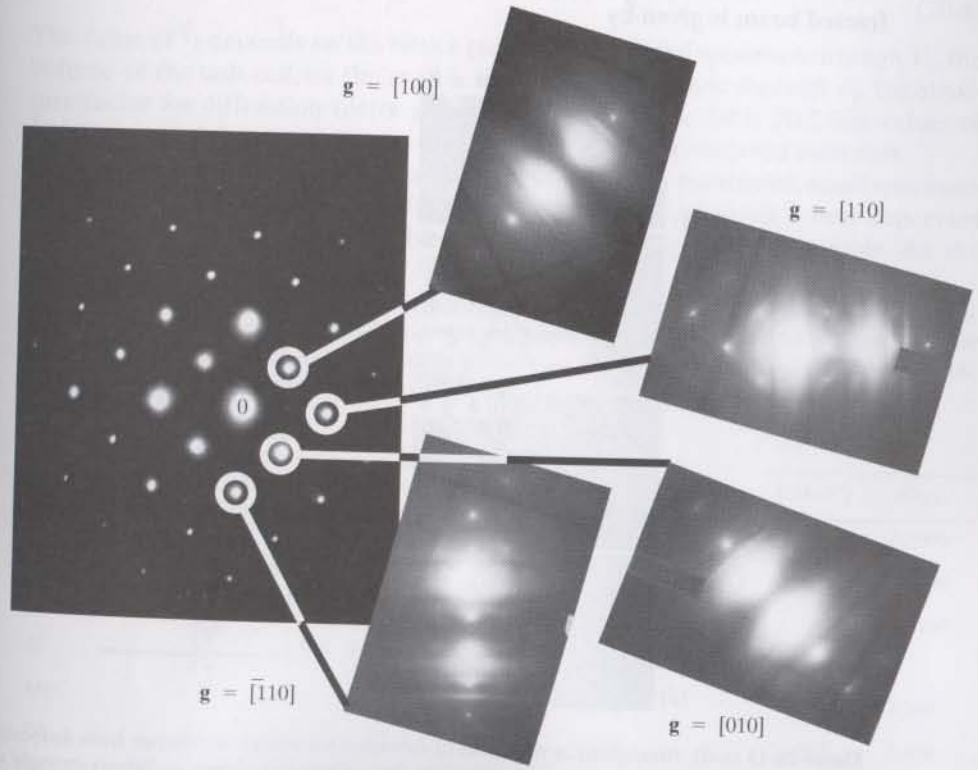


**Figure 20-12** Diffraction pattern recorded with $\mathbf{B} = [001]$ (upper left). Small tilts are used to obtain the two beam conditions shown.

An important advantage of imaging under two-beam conditions is the simplicity in calculating how different factors alter how defects appear. Also, BF and DF images show complementary contrast under conditions where absorption can be neglected. Tilting to $s \gtrsim 0$ produces best defect contrast. Remembering that high contrast describes situations where there is a large difference in signal from the feature of interest and its surroundings (Sec. 17-3), Fig. 20-13 (a)-(d) show micrographs of dislocations in NiAl for various $s$ and e) illustrates why $s$ slightly positive (i.e., the excess Kikuchi line just outside of **G**) offers best contrast. Near the dislocation core, the strain field locally distorts the planes into the Bragg condition for $\pm$ **g**. Far from the core, the planes do not satisfy the Bragg condition, and only the existence of relrods leads to any intensity being diffracted at positions away from the dislocation core. At larger $|s|$ too little of the volume around the core can diffract; while such "weak beam" imaging is useful in high resolution TEM, it typically limits its contrast too much to be desirable for everyday imaging. The fact that imaging with $s < 0$ makes the defects difficult to see is a consequence of dynamical diffraction and of absorption, and, after some development, this will be seen below.

For two-beam dynamical diffraction of electrons, the intensity $I_g$ of the Bragg diffracted beam is given by

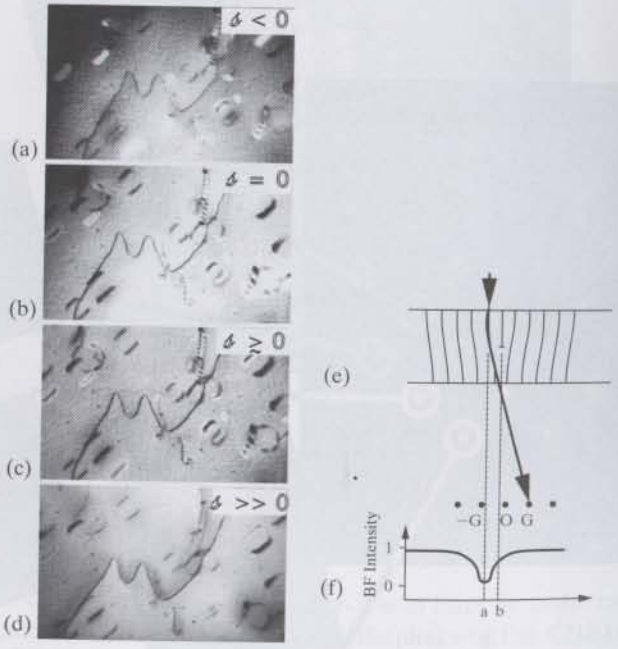


**Figure 20-13** (a-d) Illustration of the effect of deviation parameter on contrast from dislocations. (e) Local distortions around a dislocation core allow that volume to continue to diffract strongly when the crystal is tilted slightly from the exact Bragg condition. (f) Intensity profiles showing displacement of dislocation image from its projected position. (e and f after [20.2]).



$$I_g = 1 - I_0 = (\pi t/\xi_g)^2 \frac{\sin^2(\pi t s_{eff})}{(\pi t s_{eff})^2}, \tag{20-6}$$

where $I_0$ is the intensity of the incident beam, $t$ is thickness of the sample through which the electrons have traveled, $\xi_g$ is a constant called the extinction distance and has units of length and $s_{eff}$ is the effective deviation parameter given by

$$s_{eff} = \sqrt{(s^2 + \xi_g^{-2})}. \tag{20-7}$$

Note the similarity of Eq. 20-6 to the interference function defined in Eq. 5-8; also, the diffracted intensity is periodic in two independent quantities $t$ and $s_{eff}$ and the treatment neglects absorption. In the absence of absorption, Eq. 20-6 predicts that BF and DF images will be complementary.

The extinction distance $\xi_g$ can be regarded as a characteristic length for diffraction vector **g**, and this scalar quantity is given by

$$\xi_g = (\pi V_c \cos\theta_B)/(\lambda F_g). \tag{20-8}$$

The value of $\xi_g$ depends on the lattice parameter(s) of the specimen through $V_c$, the volume of the unit cell, on the atomic number of the sample through $F_g$, the structure factor for diffraction vector **g**, and the kV through $\lambda$. Table 20.2 lists values of $\xi_g$ for commonly used reflections of some frequently encountered materials.

Because diffracted intensity is a function of deviation parameter, small specimen tilts can change the appearance of images substantially. This result is very important in TEM since the foils are so thin that some bending seems inevitable. As the

**Table 20.2** (a) Values of the extinction distance $\xi_g$ (in nm) for several commonly encountered materials and diffraction vectors **g** after [20.2]. The dashes mark reflections with F=0, and all values are for 100 keV electrons. Multiplication by the correction term $v/v_{100}$, see (b), is needed to convert the values listed below to an energy E other than 100 keV [20.6].

(a)

| Material | Extinction distance $\xi_g$ | | | | |
|---|---|---|---|---|---|
| | $hkl$ = 110 | 111 | 200 | 220 | 400 |
| Al | – | 56.3 | 68.5 | 114.4 | 202.4 |
| Au | – | 18.3 | 20.2 | 27.8 | 43.5 |
| Si | – | 60.2 | – | 75.7 | 126.8 |
| MgO | – | 272.6 | 46.1 | 66.2 | 103.3 |
| Fe | 28.6 | – | 41.2 | 65.8 | 116.2 |
| W | 18.0 | – | 24.5 | 35.5 | 55.6 |

(b)

| E (keV) | $v/v_{100}$ |
|---|---|
| 30 | 0.5990 |
| 50 | 0.7528 |
| 80 | 0.9164 |
| 100 | 1 |
| 200 | 1.268 |
| 300 | 1.416 |
| 400 | 1.510 |
| 1000 | 1.717 |

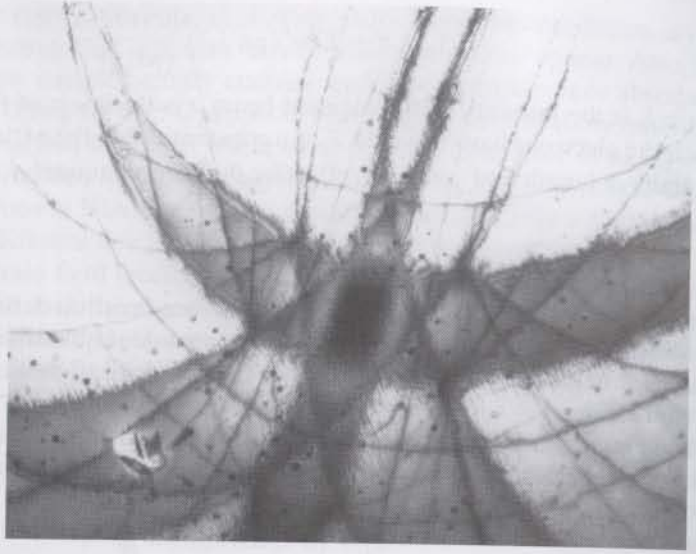

**Figure 20-14** Bend contours. (Courtesy of Z.L. Wang).

orientation in a bent sample varies with position, i.e., $s$ varies locally, diffracted intensity can change quite abruptly and the resulting bend contours can overwhelm contrast from other features. An example of bend contours appears in Fig. 20-14; these contours are often a nuisance but can also be a useful tool.

Plots of intensity $I$ vs. $s\xi_g$ are termed rocking curves and are a good way of seeing why imaging of defects is best done with $s$ slightly positive. When absorption is considered in the dynamical diffraction calculations, the BF rocking curve no longer is symmetric around $s = 0$ while the DF rocking curve remains symmetric (Fig. 20-15). In BF images, $s$ should be small and positive: better transmission and sharper images are obtained than if $s = 0$ or $s < 0$. Indeed, BF images with $s < 0$ show very low average intensity.

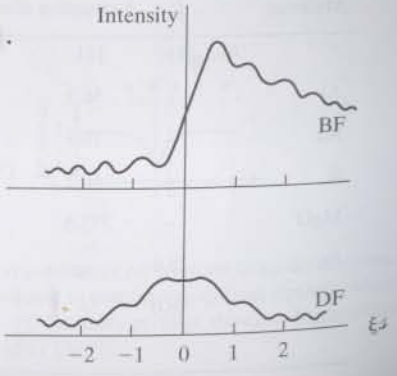


**Figure 20-15** Bright field (BF) and dark field (DF) rocking curves, very schematic (After [20.5]).



Periodicity in $t$ means that the intensity of both the **O** and **G** beams oscillates with depth below the surface on which the beam is incident. Initially $I_0$ starts at unity (it is normalized to one) and gradually decays while $I_g$ gradually increases from zero until it contains all of the intensity after traveling $\xi_g/2$ into the specimen. The process then repeats with $I_g$ decreasing while $I_0$ increases. These oscillations can be visualized as thickness fringes in wedge-shaped crystals but not in samples with constant thickness. The intensity that the **G** or **O** beam has at the exit surface dictates the intensity of that beam outside the sample, that is, when the beam is observed. It is possible, therefore, that an image may appear to be black or white depending on the thickness of the sample. Defects which might otherwise be visible in images, may not produce contrast if they lie parallel to the entrance surface of the foil and at a depth where the intensity is zero in that beam.

Defects which extend through different depths often show alternating light and dark contrast; this is a result of the oscillation in intensity between diffracted and incident beam. In dislocations this modulation in intensity is termed zig-zag contrast. In stacking faults or other planar defects alternating light and dark fringes are seen. Comparison of BF and DF images of stacking faults and other planar defects (changes of fringes from light to dark in corresponding micrographs) is an important part of identifying the character of these faults [20.2 - 20.6]. The contrast between light and dark thickness fringes in wedge-shaped crystals decreases to zero for thicknesses $t \gtrsim 5\xi_g$, and this phenomenon is also seen in contrast from stacking faults extending through foils. Explaining this effect, termed anomalous absorption in TEM and anomalous transmission in x-ray diffraction, requires referring to results from dynamical diffraction theory.

In many respects, dynamical diffraction theory for electrons and for x-rays are quite similar, and the explanations of Sec. 5-5 can be used readily for either. The interference of the two Bloch waves (for two beam conditions which are difficult to avoid for x-rays and require some effort to achieve for electrons) set up by the dynamic transfer of energy to/from the diffracted beam leads to the dependence of intensity on thickness described in Eq. 20-6. Consideration of where these Bloch waves localize spatially in the specimen reveals that the maxima in the probability distribution function for one Bloch wave coincides with the rows of atoms of the diffracting planes while that of the second centers on the channel between the planes of atoms. Because interaction between electrons of the beam and electrons of the sample's atoms leads to scattering and absorption, the former Bloch wave is heavily attenuated while the latter suffers relatively little absorption. After several $\xi_g$ of propagation only one Bloch waves remains, and the interference leading to intensity oscillation with depth disappears.

The BF images of Fig. 20-16 show several dislocations in NiAl, a material with the CsCl structure. Dislocations B and F are clearly in contrast with $\mathbf{g} = [\bar{1}10]$, [010] and [001] and cannot be seen with $\mathbf{g} = [110]$. In the $\mathbf{g} = [\bar{1}10]$ image, the contrast along the length of dislocations B and F is uniform while zig-zag contrast appears for dislocation B and for the lower right-hand portion of dislocation F in the other

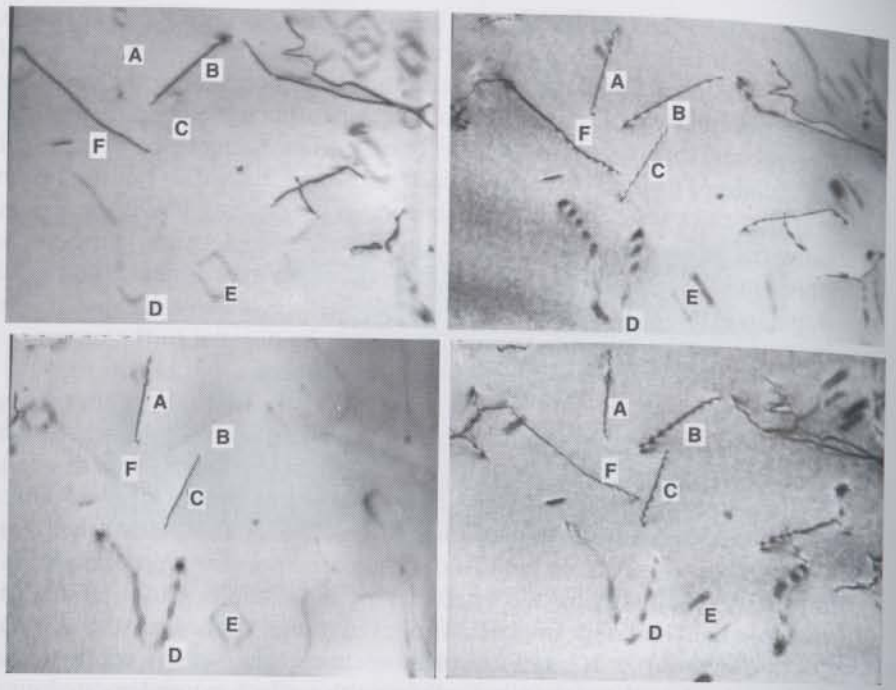


**Figure 20-16** Bright field micrographs of a NiAl sample recorded with four diffraction vectors. Identification of the Burgers vectors of dislocations **A-F** are discussed in the text. Clockwise from upper left, $\mathbf{g} = [\bar{1}10]$, [010], [100], and [110].

two images. Dislocations A and C exhibit no contrast with $\mathbf{g} = [\bar{1}10]$ and are visible in the other three BF images shown in Fig. 20-16.

Contrast of well-separated dislocation dipole D and dislocation loop E is more complex. Double images are seen for all **g** of Fig. 20-16, and this shows that the value of $\mathbf{g}\cdot\mathbf{b}$ differs for D and E compared to A, B, C, and F. Very strong zig-zag contrast of D is seen with $\mathbf{g} = [100]$. Two sides of the square loop E are completely extinct with $\mathbf{g} = [100]$ and [010] while opposite corners of the loop disappear completely with $\mathbf{g} = [110]$ and $[\bar{1}10]$. The references give more details.

When discussing whether images appear light or dark, it is important to know whether BF or DF images are under discussion. Because dislocations diffract greater intensities than the perfect regions of the crystal, there should be more intensity at the dislocation positions in DF images and less at these positions in BF images. Thus, the expected BF dislocation images in Fig. 20-12 and 20-16 consist of white lines against a dark background. In fact, this is what is seen on BF *negatives*. Printing positives from the negatives, therefore, produces dark dislocations images on a light background.



## 20-9 IMAGING AND PHASE CONTRAST

Thus far in the discussion of imaging, consideration has been limited to only one beam passing through the objective aperture. If two or more beams are allowed through the aperture, phase contrast can result. While detailed understanding of various modes of TEM phase contrast imaging requires a somewhat lengthy development (e.g., [20.2]), a straight-forward and short explanation for this type of imaging is possible [20.6].

Let the aperture allow the incident plus one diffracted beam to reach the image. The total wave function for the electrons (i.e., the amplitude) is

$$\Psi = \exp(2\pi i\mathbf{k}\cdot\mathbf{r}) + \phi_g\exp(2\pi i\mathbf{k}'\cdot\mathbf{r}), \tag{20-9}$$

where the incident wave has unit amplitude and wave vector **k** in the crystal and $\mathbf{k}' = \mathbf{k} + \mathbf{g}$ is the wave vector of the diffracted wave in the crystal. Factoring produces

$$\Psi = \exp(2\pi i\mathbf{k}\cdot\mathbf{r})[1 + \phi_g\exp(2\pi i\mathbf{g}\cdot\mathbf{r}], \tag{20-10}$$

and the intensity is, for $\phi_g = R\exp(i\delta)$,

$$I = 1 + R^2 + 2R\cos(2\pi\mathbf{g}\cdot\mathbf{r} + \delta) \tag{20-11}$$

Both R and $\delta$ are functions of $\mathcal{s}$ and thickness $t$, and from Eq. 20-6,

$$R = (\pi/\xi_g)\frac{\sin \pi t\mathcal{s}}{\pi\mathcal{s}} \tag{20-12}$$

and

$$\delta = \pi/2 - \pi t\mathcal{s} \tag{20-13}$$

Next consider how intensity varies along direction **x** (in direct space, i.e., in the image) chosen parallel to **g**, that is, in the plane normal to the incident beam **B**. Since **g** is nearly perpendicular to **B**, little error is introduced. The result of Eq. 20-11 then becomes

$$I = 1 + R^2 - 2R\sin(\{2\pi x/d\} - \pi t\mathcal{s}). \tag{20-14}$$

Thus, a modulation in intensity exists along **x** with periodicity *proportional* to $d$, a spacing in the crystal, and the lattice is "resolved" if the TEM has sufficient resolving power.

When more beams reach the image, the interference sharpens, and more details are visible in the pattern. One-dimensionally modulated lattice fringe images (from collinear diffraction spots plus the incident beam) are rarely used. More often non-collinear **G** contribute to form two-dimensional lattice fringe images

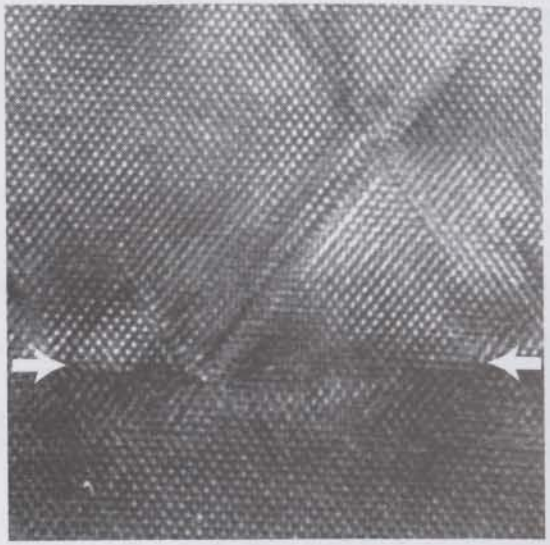

**Figure 20-17** 110 lattice fringe image of an epitaxial layer (ZnS, top) grown on a GaAs substrate; the boundary, identified with an arrow, is parallel to the bottom of the micrograph. (Courtesy Z.L. Wang.)

(Fig. 20-17).The reader should always remember that the visibility of fringes depends on orientation and on foil thickness and should never forget that individuals atoms (or even columns of atoms are not being imaged. Image simulation is often required for correct interpretation of lattice fringe and other phase contrast images. Discussion of this topic and of other interesting topics in TEM is beyond the scope of this chapter and can be found elsewhere (e.g., [20.2], [20.7], [20.8]).

# General References

**The following books are listed more or less in the order they are enco tered in the text**


G.1 *International Tables for Crystallography*, Ed. A.J.C Wilson, Vol. A (Dordrecht Kluwer Academic Pub. for International Union Crystallography, 1995). The reference "book" for crystallography and fraction.

G.2 L.S. Birks. *X-Ray Spectrochemical Analysis*, 2nd ed. (New Yo Interscience, 1969). Clear, brief treatment of wavelength and energy persive methods, with emphasis on the problems of quantitative analy Includes electron-probe microanalysis.

G.3 Duncan McKie and Christine McKie. *Essentials of Crystallograp* (Oxford: Blackwell Scientific Publications, 1986). In depth treatment crystallography, general treatment of various diffraction techniques.

G.4 Walter Borchardt-Ott. *Crystallography*, 2nd ed. (Berlin: Springer-Verl 1995). Focus is on crystallography.

G.5 Donald E. Sands. *Vectors and Tensors in Crystallography* (Reading, M Addison-Wesley Pub. Co., 1982). Quite abstract but very valuable to tho focussing on vector/tensor mathematics.

G.6 Christopher Hammond. *The Basics of Crystallography and Diffractio* International Union of Crystallography Text on Crystallography (Oxfor Oxford University Press, 1997). General coverage emphasizing crystallo raphy and general principles of diffraction. Interesting Thumbnail biogr phical sketches of important workers are included.

G.7 L.H. Schwartz and J.B. Cohen. *Diffraction from Materials*, 2nd ed. (Berli Springer-Verlag, 1987). Wider ranging thorough coverage of crystallogr phy, instruments and techniques and diffraction theory.

G.8 *Strukturbericht* (Leipzig: Akademische Verlagsgesellschaft, 1931-194 Also available from Ann Arbor, MI.: Edwards Brothers, 1943). A series seven volumes describing crystal structures whose solutions were pu lished in the years 1913 to 1939, inclusive. Continued by: *Structure Repor* (Utrecht. Oosthoek, 1951 to date). Sponsored by the International Unio of Crystallography. The volume numbers begin with Vol. 8, wher *Strukturbericht* left off. The results of structure determinations are usuall given in sufficient detail that the reader has no need to consult the origin paper.